

# A study of Mg and Cu additions on the foaming behaviour of Al-Si alloys\*

H.-M. Helwig, F. Garcia-Moreno, J. Banhart

February 27, 2011

## **Abstract**

Aluminium casting alloys containing Mg and Cu in addition to Si were investigated with respect to their potential to be foamed. The kinetics of foam expansion of different alloys was studied and the resulting structures were characterised. Of the stages of evolution of foams, namely (i) pore nucleation, (ii) foam growth in the semisolid state, (iii) further expansion in the fully liquid state, the latter two were explored. Expansion in the semisolid state could be related to the available liquid fraction. Mg-containing Al-Si alloys yielded a less coarse and more uniform pore structure than the other alloys investigated. However, achieving a high volume expansion required restriction to a narrow process window and led to the suggestion of AlMg<sub>4</sub>Si<sub>8</sub> as a practical alloy.

## **1 Introduction**

When metallic foams are made by expanding densified mixtures of metal powders and blowing agents ('PM process'), often few very large pores are observed [1].

---

\*Journal of Materials Science (submitted, 2011)

Such pores act as weak points of the structure and give rise to a large scatter of the mechanical properties. The premature gas release due to the mismatch between the decomposition temperature of the blowing agent (for aluminium alloys mostly  $\text{TiH}_2$ ) and the melting temperature of the alloy is thought to be a major reason for the inferior cell structure [1, 2, 3, 4]. One strategy to solve this problem is to delay hydrogen release from  $\text{TiH}_2$ , i.e. to shift it to higher temperatures. Heat treatments leading to partial decomposition and/or pre-oxidation of the powder surface [5, 6] or surface coatings [4, 7] have been applied. A complementary strategy is to change the alloy composition to obtain lower melting temperatures. Although this strategy appears promising, research in this field has not been very systematic. An additional motivation for the usage of alloys with a low melting temperature range is the production of 'Aluminium Foam Sandwich' (AFS), a commercially used metal foam product [8, 9]. Foaming of AFS requires melting and foaming of a core layer at low temperatures at which the material of the face sheets remains solid. As usage of high-strength but low-melting face sheet alloys is desirable for good overall mechanical performance [10], foamability of the core at low temperature is essential [11].

Al-Si alloys are well established in metal foaming. The casting alloy AlSi7 has frequently been used in the past [12, 13] and Si contents up to 12% have been reported [14]. The first PM metal foam part produced in series is made of AlSi11 [15]. A systematic study of foam expansion in the Al-Si system showed an optimum at Si contents of 6 – 7wt.% Si [16], which corresponds to  $\approx 50\%$  eutectic melt at the eutectic temperature of 577 °C. However, binary Al-Si alloys do not lead to satisfactory pore structures, which is why further alloying additions were proposed. Alloying elements that lower the melting point include Mg and Cu. Al-Si-Cu alloys have been applied in metal foaming for more than 10 years [17], mainly as foam core material for AFS sandwich panels [9, 18]. Al-Mg-Si with

low Mg and Si contents (6000 series) were studied since they can be age-hardened [19]. Further addition of up to 1 wt.% Mg to Al-Si alloys turned out to decrease the achievable volume expansion, which was ascribed to the increased oxidation rate [20]. Surprisingly, the usage of even higher Mg amounts was found to lead to promising results in the run-up to this study [21]. At present, with the development described in this work, there is a chance to replace Al-Si-Cu alloys by Al-Mg-Si casting alloys [22, 23] and in this way to reduce weight, corrosion problems and the risk of embrittlement. Zn could also be used as an addition, but due to its high solubility in Al very high contents would be required for an effective shift of the melting range. Lehmkus studied quaternary Al-Si-Cu-Zn alloys, but did not find significant improvements through Zn addition [2].

The first aim of this study is to quantitatively evaluate the potential of some new Mg-containing alloys that promise improved pore structure and higher maximum expansion. In a second step, reasons for the beneficial effect of the high Mg addition are sought. For this, the expansion behaviour as well as the pore structure development has been studied for a number of alloys.

## 2 Methods and materials

### 2.1 Precursor preparation

Figure 1 gives a schematic overview of the alloy systems investigated in more detail after a wider alloy screening had been carried out. 8 different alloys belonging to 4 alloy systems were selected. AlSi6 is the starting point, being similar to the casting alloy A357 that is sometimes used in metal foam technology [24]. This alloy is modified by adding Cu and/or Mg in the next step.

The Al-Si-Cu alloys studied are variations of alloy A319 that is in use already as a base alloy for foams [9, 18]. The rationale is to increase the amount of melt

present at the ternary eutectic temperature (525 °C) by adding copper.

Al-Mg-Si alloys with high Mg contents have not yet been considered suitable alloy candidates in the literature, where just foams based on wrought alloys of the 6000 series have been described [13, 19]. The main feature of these Mg-rich alloys is the high amount of melt available at the eutectic temperature (558 °C): It increases from 18 wt.% for AlMg6Si6 to 48 wt.% for AlMg4Si8, see Fig. 2.

By using a quaternary alloy, the solidus temperature can be further decreased. To evaluate the potential of this strategy, alloy AlMg4Si6Cu4 was also included in this study.

The different alloy compositions were realised by mixing elemental powders or master alloy powders as specified in Tab. 1 in a tumbling mixer for 15 min. In addition, the mixture contained 1 wt.% TiH<sub>2</sub> powder that had been heat-treated in air for 3 h at 480 °C to delay hydrogen evolution during foaming. Such pre-treated powder starts releasing hydrogen above about 520 °C at heating rates of 0.33 Ks<sup>-1</sup> [5], possibly at slightly higher temperatures at the faster heating rates employed in this work. Cylindrical precursor material tablets, 36 mm in diameter, 7 mm high and weighing 20 g, were produced by uniaxial pressing applying 300 MPa compaction pressure first at 20 °C for a few seconds and then at 400 °C compaction temperature for 300 s.

## 2.2 Measurement of foam expansion

Foam expansion was measured in a special dilatometer (so-called 'expandometer') that was designed for in-situ metal foam expansion measurements. The instrument used was originally built at the Institute of Materials and Machine Mechanics of the Slovak Academy of Sciences, but was then modified to allow for a more precise sample temperature control and monitoring [21]. It consists of an infrared furnace and a cylindrical glass mold open only at the top in which the tablet is foamed.

The mould accommodates a movable piston connected to a position sensor used to monitor foam expansion. The foaming atmosphere was air. The temperature program comprised first a heating phase applying a given constant heating power, resulting either in  $2.6 \text{ Ks}^{-1}$  or  $1.2 \text{ Ks}^{-1}$  heating rate (determined at  $500^\circ\text{C}$ ) up to a final temperature of  $630^\circ\text{C}$  and then a stage of constant temperature for 300s to allow for foam expansion. The higher heating rate represents the upper limit that can be achieved with the expandometer setup. The lower value is typical for practical foaming. Much lower values have a negative impact on foaming [28] but are irrelevant in the context of the present work. The thermocouple used for measuring the foam temperature protruded into the sample through the sample support from below.

The measured data was either displayed as volume expansion versus time or converted into expansion versus melt fraction by using the known sample temperature at any instant and applying the commercial software **JMatPro** that allows for calculating phase diagrams [25, 26] using the CALPHAD approach, a Gibbs energy minimising method based on experimental data bases [27]. Figure 2 shows data for the melt fraction of various alloys as a function of temperature as calculated by this approach.

For alloys that isothermally melt at the eutectic temperature, the eutectic melt fraction  $x_E(t)$  at a time  $t$  between the beginning and the end of isothermal melting ( $t_1$  and  $t_2$ ) was linearly interpolated using the maximum possible amount of eutectic melt  $x_E(t_2)$  and assuming a constant heat flux  $\dot{Q}$  into the sample, i.e. neglecting possible changes of the heat transfer conditions due to sample expansion:

$$x_E(t) = x_E(t_2) \left( 1 - \frac{t_2 - t}{t_2 - t_1} \right) \quad (1)$$

Since data for the density of the liquid fraction in the semisolid state is not available

for the alloys used, the exact volume fraction of the melt is not known. However, by using weight fractions instead, just a small error is caused for the system Al-Mg-Si.

We determined two expansion rates, one in the range between the particular liquidus temperature and the final temperature (630 °C) and one during the following isothermal stage at 630 °C. After the experiment, cooling of the sample was initiated by turning off the furnace. The initial cooling rate was typically 1 K/s.

### 2.3 Structure characterization

In-situ X-ray radiography was performed using a microfocus X-ray tube as described in Ref. [28]. The samples were 20 mm wide, 7 mm high and 5 mm thick, with the compaction (and expansion) direction arranged vertically and perpendicular to the beam direction.

Foam structure was characterised by analysing polished sections of slightly expanded foams of the different alloys using a Zeiss Axiophot 2 microscope. Pore counting was done using the free image analysis software `ImageTool` [29]. The minimum pore cross section that could be analysed was  $450 \mu\text{m}^2$ . Due to the constant analysed area of  $2.8 \text{ mm} \times 2.2 \text{ mm}$  it was necessary to correct for the different sample porosities  $P$  to obtain a number of pores  $N_P$  related to the same initial cross section of the precursor before foaming. Therefore,  $N_P$  was determined from  $N_{P,\text{measured}}$  that represents the actual counted number by using

$$N_P = \frac{N_{P,\text{measured}}}{1 - P}. \quad (2)$$

Highly expanded foam samples from the expandometry measurements were sectioned parallel to the expansion (compaction) axes and the foam structure was scanned using a document scanner after filling the pores with a contrast enhancer [30]. Pore size distributions were again obtained using `ImageTool`. The minimum

cross section required for safe pore identification was  $1 \text{ mm}^2$  in this case.

## 3 Results

### 3.1 Foam expansion

Figure 3 displays the temperature and volume expansion course of the alloy AlMg4Si6 for both heating rates applied in this study. The solidus and liquidus temperatures,  $T_S$  and  $T_L$ , are clearly correlated to kinks in the temperature course ('A' and 'B'). Below the solidus temperature, no foam expansion is observed and just the thermal expansion of both the sample and instrument gives rise to a slight linear increase. After  $T_S$  has been reached, foam expansion sets in. For all the alloys investigated, the expansion rates depend on the heating rate. Shortly before reaching the final temperature of  $630^\circ\text{C}$ , the expansion rate for the high heating rate (slope 1 in Fig. 3) largely exceeds the expansion rate at the low heating rate (slope 3). After being at the final temperature, the expansion rates immediately drop to lower values (slopes 2 and 4 in Fig. 3).

In Fig. 4, the expansion is shown as a function of temperature. Here, expansion is nearly independent of the heating rate. The calculated melt fraction as a function of the temperature and the two expansion curves show a clear similarity, which suggests to compare volume expansion as a function of melt fraction for various alloys, see Fig. 5. In this representation, foam volume increases monotonically with the melt fraction for all the alloys. Only the two expansion curves of the Cu-containing alloys show a slightly delayed expansion compared to the other alloys in the region up to 50% melt fraction. The degree of expansion after reaching  $T_L$  is very similar for all the alloys except for AlMg6Si6 where expansion at melt fractions  $>50\%$  has largely slowed down.

All the maximum foam expansions are compared in Fig. 6. The highest expan-

sion values were assumed by alloys AlSi6 and AlMg4Si8. The values achieved by the Al-Si-Cu alloys are just slightly lower for the high and on the same level for the low heating rate. Within the Al-Si-Cu alloy series there is no significant trend as a function of Cu content. The Al-Si-Cu alloys show the same maximum expansion for the two heating rates applied, while all the other alloys expand slightly more at high heating rates. Unlike Al-Si-Cu, the Al-Mg-Si alloy system exhibits a trend of higher maximum expansion with a higher amount of eutectic melt produced isothermally during foaming. The decrease of this eutectic melt fraction from 48 % for AlMg4Si8 to 18 % for AlMg6Si6 is associated with a decrease of maximum expansion of  $\approx 30\%$ . The quaternary alloy AlMg4Si6Cu4 and alloy AlMg6Si6 show the lowest expansions of all the alloys studied.

The expansion rates of the different alloys in the range between the liquidus temperature and the final temperature (630 °C) are compared in Fig. 7(a). These values correspond to slopes 1 and 3 in Fig. 3. Experiments made with high heating rate produce a significantly higher expansion rate than the ones with low rate. No clear dependence on the alloy composition or the melting temperature range is visible.

The expansion rates determined during expansion at constant temperature (630 °C) are given in Fig. 7(b) (slopes 2 and 4 in Fig. 3). Here, the heating rate has no obvious influence, i.e. after being at the final temperature, the rate at which this temperature was reached played no role any more. The expansion rates in this stage are low for all the alloys, ranging from  $0.015 \text{ mm}\cdot\text{s}^{-1}$  to  $0.055 \text{ mm}\cdot\text{s}^{-1}$ , and for alloy AlMg4Si6Cu4 the expansion rate is close to zero. As seen from Fig. 7, for all the alloys, the expansion rates decrease sharply after the isothermal stage has been reached. This change is more pronounced for the higher heating rate.



### 3.2 Development of pore structure

For one of the alloys, Fig. 8(a) shows the pore structure in early foaming stages. The first step of evolution is the nucleation of many small individual pores that then start to grow. Most of them are nearly equiaxed and have a preferred orientation that can be determined using quantitative analysis. The pores often arrange into linear arrays, see (2), that more frequently appear to be oriented perpendicular to the compaction axis, although other orientations can also occur. The pores in these arrays merge to larger elongated pores in a later stage, see (1). In Fig. 8(b), a closeup shows such an array in a different alloy, see (3). Here, the material between the pores of the array had been partially liquid, while mainly pore-free areas in the direct vicinity of the pore array show no sign of prior melting.

The number of detected pores related to the original precursor volume is given in Fig. 9. A maximum value of the number of such pores is observed for 2D-porosities of 20%-25%. Mg-containing alloys have significantly more pores in the region of 10%-25% 2D-porosity than Mg-free ones.

X-ray images of the foams in an early stage after pore nucleation as shown in Fig. 10 reveal cracks that propagate horizontally, i.e. perpendicular to the compaction direction for 30% expansion. The pores in the AlMg4Si6 alloy appear less cracklike than in AlSi6Cu4 or even AlSi6. In the latter case of a AlSi6 alloy, visible cracks lengths can reach  $\approx 1$  cm (50% of the sample width). The crack-like structure of the early-stage pores results in an anisotropic expansion after they get inflated by the blowing gas since they then expand perpendicular to their orientation, i.e. parallel to the compaction direction. The particular alloys show different characteristics of anisotropy of expansion even in a later stage (area expansion 100%, Fig. 10(b)), where the stronger anisotropy of expansion compared to the other alloys leads to a nearly rectangular contour of the AlSi6 sample. AlSi6Cu4 shows a rounder shape due to less anisotropic expansion, while the AlMg4Si6 foam

is the roundest.

Statistical averages of macroscopic pore cross sections in fully expanded foams including pores exceeding 1 mm<sup>2</sup> area are given in Fig. 11. The  $Pn$ -values specified indicate the cell area a fraction of  $n\%$  of the pores (by number) does not exceed ( $P50$  is then the median value). The span between  $P95$  and the maximum values of the distributions is a measure for the homogeneity of the pore structure since it reflects the presence or absence of very large individual pores. Such differences are especially small for the alloy AlMg4Si8. The absolute values of the other parameters indicate whether the structure formed by the majority of the pores is coarse or fine. One can identify the following ranking for the coarseness of the structure:

$$\boxed{\text{coarse}} \leftarrow \text{AlSi6} > \underbrace{\text{AlSiCu}}_{3 \text{ alloys}} >> \underbrace{\text{AlMgSi}}_{3 \text{ alloys}} > \text{AlMg4Si6Cu4} \rightarrow \boxed{\text{fine}} \quad (3)$$

The biggest difference is found between the group of the Mg-free (4 left in Fig. 11) and Mg-containing alloys (4 right in Fig. 11).

## 4 Discussion

It was found that by using Mg as an alloying element, less coarse and more homogeneous Al-Si-based foams can be manufactured (Fig. 11). However, Mg can also have an adverse effect on expansion if used in the wrong proportion to other elements, as the expansion measurements showed (Fig. 6). Therefore, a trade-off between beneficial and adverse effects of Mg has to be considered. These effects shall be discussed in the following. The alloy AlMg4Si8 represents a good compromise due to the good expansion and fine pore structure found (Fig. 6, Fig. 11) and Fig. 13, which is why this alloy has been further studied [22, 23].

Figure 5 shows that during melting of the alloy foam expansion is rather correlated with the melt fraction than with the temperature. Different alloys reach the same melt fraction at different temperatures, see Fig. 2, which is why diagrams such as Fig. 4 show initial foam expansion at different temperatures for different alloys. In contrast, in Fig. 5, the different alloys show a similar course with only few deviations: The delay for the Cu-containing alloys between 30% and 50% melt fraction could be an artefact, as in the powder compacts containing Cu powder local melting around individual powder particles produces a lot of eutectic melt at lower temperatures, but this melt is contained in local pockets at the location of former copper particles [31]. Oxide layers around the former powder particles could hamper the equalisation of concentration gradients. The actual global melt fraction can therefore be lower than the value determined from the equilibrium phase diagram and used in Fig. 5. A correction for this would move the curves in the direction of the arrow given in Fig. 5, but this correction cannot be quantified. As Mg is already dissolved in the AlMg50 master alloy used, no such local melting is observed in the Al-Mg-Si alloys. Since Mg also helps breaking the oxide films during powder pressing, Mg powder compacts melt more homogeneously.

The decomposition rate of the blowing agent strongly depends on temperature [5, 32, 33, 34]. Therefore, the correlation found between melt fraction and expansion – even though not perfect – is not trivial. The volume gain of the foam in the semisolid melting range is limited by the extent to which the matrix can be stretched and accommodate gas bubbles, and this ability increases with the liquid fraction. Gas supply at this stage is necessary but not a controlling factor. Only after complete melting, further foaming will be largely controlled by the strongly temperature-dependent gas release from the blowing agent.

An important aspect in this foaming stage is the development of the pore structure. Expanded foams in the liquid can be very stable [35, 36] unless the

temperature exceeds a critical value [37]. But even if the temperature is controlled properly, coalescence can always be observed in expanding foams, clearly visible in in-situ X-ray images as rupture of films separating adjacent bubbles [11, 28, 37, 38]. In this work, we show that coalescence takes place already in very early stages. The structure of just slightly expanded samples as displayed in Fig. 8 shows that pore coalescence already occurs on the microscopic scale below 30% porosity. X-ray radiography cannot reveal such processes in the still rather dense structure. Fig. 9 shows that for large porosities the number of pores exceeding an area of  $450 \mu\text{m}^2$  is still increasing, which means that smaller pores are inflated to such an extent that they are counted (the actual nucleation process takes place at much smaller length scales and is not reflected by our image analysis). The peak in pore number observed in Fig. 9 indicates that after a certain level of porosity has been reached ( $\approx 25\%$ ), the coalescence rate exceeds the rate at which countable pores are being generated and the total number of pores decreases. In 2D images, coalescence appears as the merger of linear pore arrays. Due to the symmetry with respect to the compaction axis there is good reason to assume that these observed arrays are in reality planar structures in 3D [39].

While the merger of small pores at this stage exhibits no clear preferential direction, X-ray analysis of the same materials in later stages, see Fig. 10, shows oriented crack-like structures as a result of anisotropic processes, in agreement with previous findings [38, 39, 40]. Pore growth that resembles crack propagation as observed in the semisolid state is often ascribed to the temperature mismatch between  $\text{TiH}_2$ -decomposition and melting [1, 2, 3, 4]. This leads to a build-up of gas pressure already in the solid or semisolid state in which the metal cannot form expanding bubbles. In this stage, foam expansion is anisotropic.

Compared to  $\text{AlSi6}$ , both Cu and Mg additions reduce the formation of crack-like structures, but the addition of magnesium has a stronger influence than that

of copper, see Fig. 10. At first sight, this appears counter-intuitive, as the solidus temperature is shifted to a lower level by Cu (525 °C) than by Mg (558 °C), i.e. melt is provided at the lowest temperatures in Cu-containing alloys. However, not only the temperature but also the amount of melt that is produced after exceeding the ternary eutectic temperature matters and phase diagram analysis indeed shows that the melt fraction achieved at the solidus temperature of Al-Mg-Si alloys (558 °C) is much higher than that of the Al-Si-Cu alloys (525 °C) at the analogous temperature, see Fig. 2.

Knowing this, the model illustrated schematically in Fig. 12 is proposed. Based on the microstructural investigations we assume that in the melting range islands of still solid material are bridged by both solid and liquid material of smaller cross section. During further heating, the latter grow at the expense of the former. Caused by the increasing pressure provided by the blowing agent, two different types of pore coalescence are possible: rupture of solid bridges that occurs preferentially in the pressing direction and rupture of liquid films that occurs isotropically. The reason for the lower strength of the still solid material in the vertical direction is that this is also the pressing direction of the powder. Strength-reducing oxide films are thought to remain unchanged when faying surfaces are pressed against each other, while the oxides are fragmented when powder particles slide against each other. This gives rise to a lower strength in the pressing direction.

In Al-Si-Cu alloys, melt is formed at 525 °C, but only in small amounts. This weakens the structure considerably. The small amount of eutectic melt, see Fig. 2, is first confined to small pockets and later spreads along the grain boundaries [31]. It cannot bridge the solid constituents that are pushed apart by the gas which in turn gives rise to crack formation. This appears as an analogue to hot-tearing in many Al alloys containing low amounts of eutectic melt, although that effect occurs during solidification [41]. In Al-Mg-Si alloys, the matrix remains its solid integrity

up to 558 °C. The integrity of the matrix is further strengthened by the presence of Mg since it helps breaking the oxide films covering the individual powder particles during hot pressing and sintering [42]. At 558 °C, a large amount of eutectic melt is generated isothermally and liquid films dominate quickly. Other than solid bridges, liquid films are stretchable and are able to stop crack propagation and prevent coarsening of the structure in the semisolid state.

In addition to their effect on the melting temperature, alloying elements, first of all Mg, modify melt properties such as viscosity, surface tension and affinity to oxidation. Surface tension is a potential driving force for cell wall rupture. All alloying elements used reduce the surface tension of Al [43], but the influence of Mg is much higher than the effect of other elements. Mg could therefore be beneficial for film stabilisation for this reason, especially as it enriches at the surface [44].

Oxide skins or particles at the metal/gas interface play a crucial role for metal foam stability [16, 35, 45, 46, 47]. During expansion, oxide skins repeatedly rupture, but new oxides form, preferably at the thinnest point of the oxide skin [41]. Oxygen is present in the precursor as air entrapped during compaction or as adsorbate on the powder surfaces (mainly H<sub>2</sub>O and hydroxides) [48, 49]. In both cases, Al and Mg can react with oxygen [50]. Another influence of oxidation (beside that on film stability) is the mechanical resistance of the oxidised inner surfaces against expansion [47]. The smaller the pores, the higher the inner surface and hence the resistance. The quaternary alloy with the smallest pores, see Fig.11, and the alloy containing 6 wt.% Mg both have a poor maximum expansion, see Fig. 6. The quaternary alloy even shows a complete loss of expansion rate after full melting, see Fig. 7(b). This underlines that a high Mg content in conjunction with small pores restricts foam expansion. On the other side, the coarse structure of AlSi6 foam explains the high expansion reached (Fig. 6).

Melt viscosity is an often discussed possible influence factor for cell wall stabil-

ity, although recent microgravity research showed no significant gain in stability in the absence of drainage [36]. Unfortunately, the viscosity of the liquid in the films of a semisolid foam can hardly be quantified. Known is just the ability of Mg-containing alloys to form finely dispersed stable solid  $\text{Mg}_2\text{Si}$  particles in the relevant temperature region, which could lead to an increased apparent viscosity of the melt [51]. Such  $\text{Mg}_2\text{Si}$  particles have actually been found in solidified samples [21].

The present paper mainly deals with foam expansion in the melting range of the base alloy, but the stages before and after are equally important. The entire foaming process can be subdivided into:

- the nucleation stage in which the initial pores are created. Nucleation is observed only indirectly in the present work,
- the melting stage in which the fraction of already melted material mainly determines foam expansion. In this stage, the foundation has to be laid for a uniform pore structure and a further smooth and high expansion,
- the expansion stage of the fully liquid alloy, which is strongly influenced by the characteristics of  $\text{TiH}_2$  decomposition. As soon as the temperature increase comes to an end, foam expansion slows down or even stops since further gas evolution can only be triggered by increasing temperatures.

At present, a thorough investigation of the nucleation stage is lacking in the literature. Only few studies have been carried out, e.g. using ultra-small scattering techniques or electron microscopy [52]. Gathering further information should be the subject of further work.

## 5 Conclusions

- Mg and Cu additions to Al-Si alloys can improve both the pore structure and the maximum expansion.
- Mg shows clear advantages over Cu as third alloying element.
- The alloy AlMg4Si8 represents a good trade-off between the beneficial effects of Mg and adverse factors.
- The beneficial action of Mg is to provide a high melt fraction at the solidus temperature and possibly also to decrease both surface tension and viscosity. Moreover, Mg improves sintering during powder pressing.
- The proneness of Mg to oxidation could help to stabilise the foams but can also hinder foam expansion.
- Foam expansion in the semisolid range is directly correlated to melt fraction.
- Pore coalescence was found to start very early, i.e. at <10% pore fraction, and to reduce the number of pores above 25% pore fraction.

## References

- [1] B. Matijasevic and J. Banhart. Improvement of aluminium foam technology by tailoring of blowing agent. *Scripta Materialia*, 54:503–508, 2006.
- [2] D. Lehmhus and M. Busse. Potential new matrix alloys for production of PM aluminium foams. *Advanced Engineering Materials*, 6:391–396, 2004.
- [3] A. Ibrahim, C. Körner, and R.F. Singer. The effect of TiH<sub>2</sub> particle size on the morphology of Al-foam produced by PM process. *Advanced Engineering Materials*, 10:845–848, 2008.



- [4] P.M. Proa-Flores and R.A.L. Drew. Production of aluminum foams with Ni-coated TiH<sub>2</sub> powder. *Advanced Engineering Materials*, 10:830–834, 2008.
- [5] B. Matijasevic, J. Banhart, S. Fiechter, O. Görke, and N. Wanderka. Modification of titanium hydride for improved aluminium foam manufacture. *Acta Materialia*, 54:1887–1900, 2006.
- [6] D. Lehmus and G. Rausch. Tailoring titanium hydride decomposition kinetics by annealing in various atmospheres. *Advanced Engineering Materials*, 6:313–330, 2004.
- [7] Z. Yang, J. Fang, and B. Ding. Effect of SiO<sub>2</sub> coating layer morphology on TiH<sub>2</sub> gas release characteristic. *Journal of Colloid and Interface Science*, 290:305–309, 2005.
- [8] H.-W. Seeliger. Manufacture of aluminum foam sandwich (AFS) components. *Advanced Engineering Materials*, 4:753–758, 2002.
- [9] pohltec metalfoam GmbH. Homepage of pohltec metalfoam GmbH (Köln, Germany). <http://www.metal-foam.de>.
- [10] D. Lehmus, M. Busse, Y. Chen, H. Bomas, and H.-W. Zoch. Influence of core and face sheet materials on quasi-static mechanical properties and failure in aluminium foam sandwich. *Advanced Engineering Materials*, 10:863–867, 2008.
- [11] J. Banhart, H. Stanzick, L. Helfen, T. Baumbach, and K. Nijhof. Real-time X-ray investigation of Aluminium Foam Sandwich production. *Advanced Engineering Materials*, 3:407–411, 2001.
- [12] W. Brinkers and J. Banhart. Fatigue behaviour of metallic foams. *Journal of Materials Science Letters*, 18:617–619, 1999.

- [13] I. Duarte and J. Banhart. A study of aluminium foam formation — kinetics and microstructure. *Acta Materialia*, 48:2349–2362, 2000.
- [14] J. Banhart, M. Weber, and J. Baumeister. Damping properties of aluminium foams. *Materials Science and Engineering*, A205:221–228, 1996.
- [15] Alulight International GmbH. Homepage of Alulight International GmbH (Ranshofen, Austria). <http://www.alulight.com>.
- [16] P. Weigand. *Untersuchung der Einflussfaktoren auf die pulvermetallurgische Herstellung von Aluminiumschaum*. PhD thesis, RWTH Aachen, Aachen, Germany, 1999.
- [17] J. Banhart and J. Baumeister. Deformation characteristics of metal foams. *Journal of Materials Science*, 33:1431–1440, 1998.
- [18] S. G. Shabestari, N. Wanderka, W. Seeliger, and J. Banhart. Optimisation of the strength of aluminium foam sandwich (AFS) panels by different heat treatments. *Materials Science Forum*, 519-521:1221–1226, 2006.
- [19] D. Lehnhus, J. Banhart, and M.A. Rodriguez-Perez. Adaption of aluminium foam properties by means of precipitation hardening. *Materials Science and Technology*, 18:474–479, 2002.
- [20] F. Simancik, K. Behulova, and L. Bors. Effect of ambient atmosphere on metal foam expansion. In J. Banhart, M.F. Ashby, and N.A. Fleck, editors, *Cellular Metals and Metal Foaming Technology*, pages 89–92, 2001.
- [21] H.-M. Helwig. *Einfluss von Verdichtungsparametern und Legierungselementen auf das Schäumverhalten von Aluminiumpulverpresslingen*. PhD thesis, Technische Universität Berlin, Berlin, 2009.

- [22] H.-M. Helwig, J. Banhart, and H.-W. Seeliger. Aluminiumlegierung für Metallschäume, ihre Verwendung und Verfahren zur Herstellung. German patent application 10 2008 027 798.3, patent pending, 2008.
- [23] H.-M. Helwig, S. Hiller, F. Garcia-Moreno, and J. Banhart. Influence of compaction conditions on the foamability of AlSi8Mg4 alloy. *Metallurgical and Materials Transactions B*, 40:755–767, 2009.
- [24] F. Baumgärtner, I. Duarte, and J. Banhart. Industrialisation of powder compact foaming process. *Advanced Engineering Materials*, 2:168–174, 2000.
- [25] N. Saunders. The modelling of stable and metastable phase formation in multi-component Al-alloys. In J.F. Nieh, A.J. Morton, and B.C. Muddle, editors, *Proc. 9th Int. Conf. on Aluminium Alloys (ICAA9)*, pages 96–106, 2004.
- [26] Sente Software Ltd. Practical software for materials properties JMatPro. <http://www.sentesoftware.co.uk>.
- [27] U.R. Kattner. Thermodynamic modeling of multicomponent phase equilibria. *Journal of Metals*, 49:14–19, 1997.
- [28] F. Garcia-Moreno, M. Fromme, and J. Banhart. Real-time X-ray radioscopy on metallic foams using a compact micro-focus source. *Advanced Engineering Materials*, 6:416–420, 2004.
- [29] University of Texas Health Science Center. Homepage of UTHSCSA Image-Tool. <http://ddsdx.uthscsa.edu/dig/itdesc.html>.
- [30] T. Wübben. *Zur Stabilität flüssiger Metallschäume - Untersuchung des Einflusses fester Partikel auf den Schaumbildungsprozess unter variierten Schwerkraftbedingungen*. PhD thesis, Universität Bremen, Bremen, 2003.

- [31] A. Rack, H.-M. Helwig, A. Rueda, B. Matijasevic-Lux, J. Banhart, L. Helfen, T. Baumbach, and J. Goebbels. Early pore formation in aluminium foams studied with ex-situ synchrotron micro-tomography and 3D image analysis. *Acta Materialia*, 57:4809–4821, 2009.
- [32] F. von Zeppelin, M. Hirscher, H. Stanzick, and J. Banhart. Desorption of hydrogen from blowing agents used for foaming metals. *Composite Science and Technology*, 63:2293–2300, 2003.
- [33] A.R. Kennedy and V.H. Lopez. The decomposition behaviour of as-received and oxidised TiH<sub>2</sub> foaming agent powder. *Materials Science and Engineering*, A357:258–263, 2003.
- [34] V. Bhosle, E.G. Baburaj, M. Miranova, and K. Salama. Dehydrogenation of TiH<sub>2</sub>. *Materials Science and Engineering A*, 356:190–199, 2003.
- [35] C. Körner, M. Arnold, and F. Singer. Metal foam stabilisation by oxide network particles. *Materials, Science & Engineering A*, 396:28–40, 2005.
- [36] F. Garcia-Moreno, C. Jimenez, M. Mukherjee, P. Holm, J. Weise, and J. Banhart. Experiments on metallic foams under gravity and microgravity. *Colloids and Surfaces A*, 344:101–106, 2009.
- [37] H. Stanzick, M. Wichmann, J. Weise, L. Helfen, T. Baumbach, and J. Banhart. Process control in aluminum foam production using real-time X-ray radiography. *Advanced Engineering Materials*, 4:814–823, 2002.
- [38] J. Banhart, H. Stanzick, L. Helfen, and T. Baumbach. Metal foam evolution studied by synchrotron radiography. *Applied Physics Letters*, 78:1152–1154, 2001.

- [39] M.A. Rodriguez-Perez, E. Solorzano, J.A. de Saja, and F. Garcia-Moreno. The time-uncoupled aluminium free-expansion: Intrinsic anisotropy by foaming under conventional conditions. In L.-P. Lefebvre, J. Banhart, and D. Dunand, editors, *Porous Metals and Metal Foaming Technology*, pages 75–78, Pennsylvania, 2008. DEStech Publishing.
- [40] L. Helfen, T. Baumbach, H. Stanzick, J. Banhart, A. Elmoutaouakkil, and P. Cloetens. Viewing the early stage of metal foam formation by computed tomography using synchrotron radiation. *Advanced Engineering Materials*, 4:808–813, 2002.
- [41] J. Campbell. *Castings*. Butterwoth-Heinemann, second edition, 2003.
- [42] A.A. Shirzadi, H. Assadi, and E.R. Wallach. Interface evolution and bond strength when diffusion bonding materials with stable oxide films. *Surface and Interface Analysis*, 31:609–618, 2001.
- [43] S.-H. Park, B.-Y. Hur, S.-Y. Kim, D.-K Ahn, and D.-I. Ha. A study on the viscosity and surface tension for Al foaming and the effects of addition elements. In C.-P. Hong, D.-H. Kim, and K.-Y. Kim, editors, *Proceedings of the 65th World Foundry Congress Gyeongju, Korea*, pages 515–523, 2002.
- [44] O.E. Awe, O. Akinlade, and L.A. Hussain. Bulk and surface properties of liquid Al-Mg, Au-Sn, and Mg-Ti compound forming alloys. *Surface Science*, 600:2122–2128, 2006.
- [45] G. Kaptay. Interfacial criteria for stabilization of liquid foams by solid particles. *Colloids and Surfaces A*, 230:67–80, 2004.
- [46] T. Wübben and Odenbach. Stabilisation of liquid metallic foams by solid particles. *Colloids and Surfaces A*, 266:207–213, 2005.

- [47] A. Dudka, F. García-Moreno, N. Wanderka, and J. Banhart. Structure and distribution of oxides in aluminium foam. *Acta Materialia*, 56:3990–4001, 2008.
- [48] F. Garcia-Moreno and J. Banhart. Foaming of blowing agent free aluminium powder compacts. *Colloids and Surfaces A*, 309:264–269, 2007.
- [49] C. Jimenez, F. Garcia-Moreno, J. Banhart, and G. Zehl. Effect of relative humidity on pressure induced foaming (PIF) of aluminium-based precursors. In L.P. Lefebvre, J. Banhart, and D. Dunand, editors, *Porous Metals and Metal Foaming Technology*, pages 59–62, Pennsylvania, 2008. DEStech Publishing.
- [50] N. Birks and G.H. Meier. *Introduction to High Temperature Oxidation of Metals*. Edward Arnold Ltd, London, 1983.
- [51] M. Paes and E.J. Zoqui. Semi-solid behaviour of new Al-Si-Mg alloys for thixoforming. *Materials Science and Engineering A*, 406:63–73, 2005.
- [52] J. Banhart, D. Bellmann, and H. Clemens. Investigation of metal foam formation by microscopy and ultra small-angle neutron scattering. *Acta Materialia*, 49:3409–3420, 2001.

## Tables

Table 1: List of powders used.

type	supplier	purity [wt.%]	D <sub>10</sub> [ $\mu\text{m}$ ]	D <sub>50</sub> [ $\mu\text{m}$ ]	D <sub>90</sub> [ $\mu\text{m}$ ]
Al	Alpoco Ltd. UK	99.7	16.4	38.2	75.5
AlMg50	Possehl Erzkontor GmbH, Germany	n.sp.	6.7	33.4	72.1
Cu	Chempur GmbH, Germany	99.7	9.6	26,5	53
Si	Elchem ASA	99.5	7	25.7	50
TiH <sub>2</sub>	Chemetall GmbH Germany	98.8	3.2	14.4	34.2

# Figures

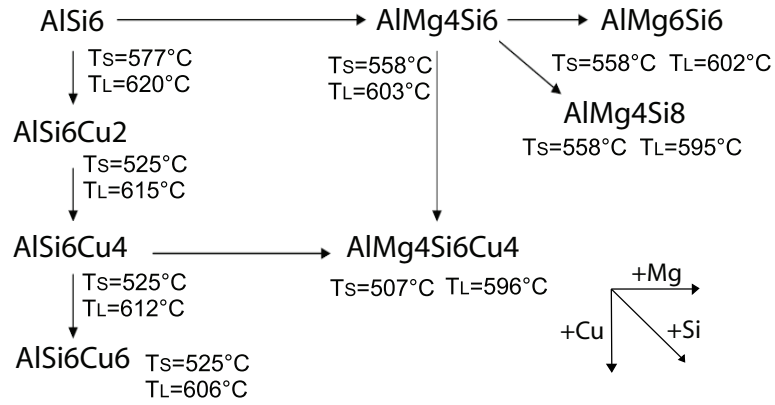


Figure 1: Strategy of alloy optimisation based on adding Mg, Cu or Si to the starting alloy  $\text{AlSi}_6$ . Solidus ( $T_S$ ) and liquidus ( $T_L$ ) temperatures of the individual alloys are calculated values [26]. The diagonal arrow for Si points into the third dimension.



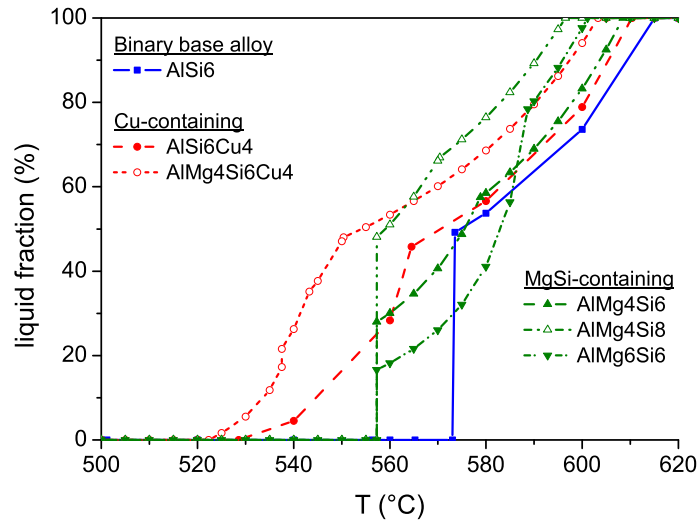


Figure 2: Liquid fractions as a function of temperature for different alloys. Calculations were carried out using the software JMatPro [26].

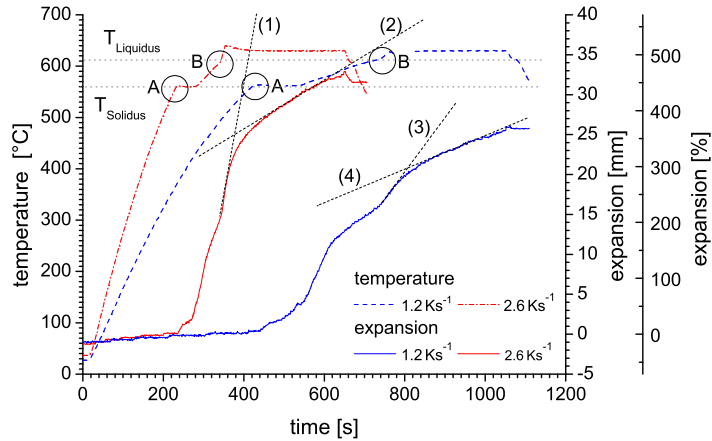


Figure 3: Temperature and expansion curves for alloy AlMg4Si6 foamed at two different heating rates. Broken lines labelled (1) to (4) mark expansion rates in different foaming stages. The solidus and liquidus temperatures  $T_S$  and  $T_L$  are marked by horizontal lines, the heat effects observed at these temperatures by letters 'A' and 'B'.

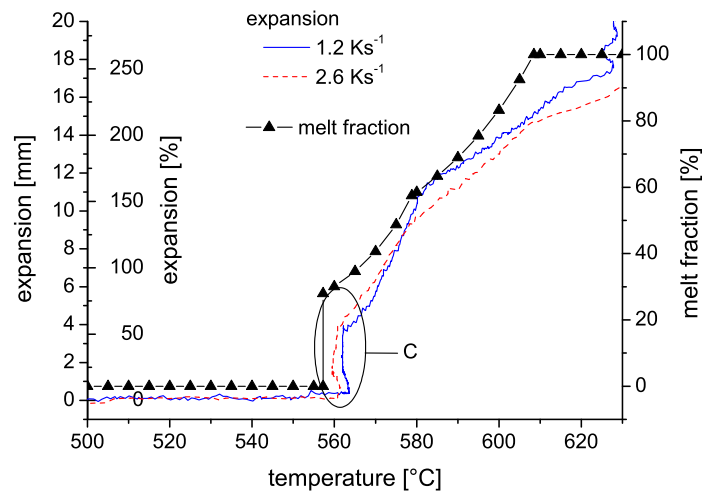


Figure 4: Expansion curves for AlMg4Si6 as taken from Fig. 3 but displayed as a function of temperature up to  $T = 630\text{ }^{\circ}\text{C}$ . Triangles: melt fraction calculated with the software JMatPro. 'C' marks artefacts caused by varying heat contact conditions.

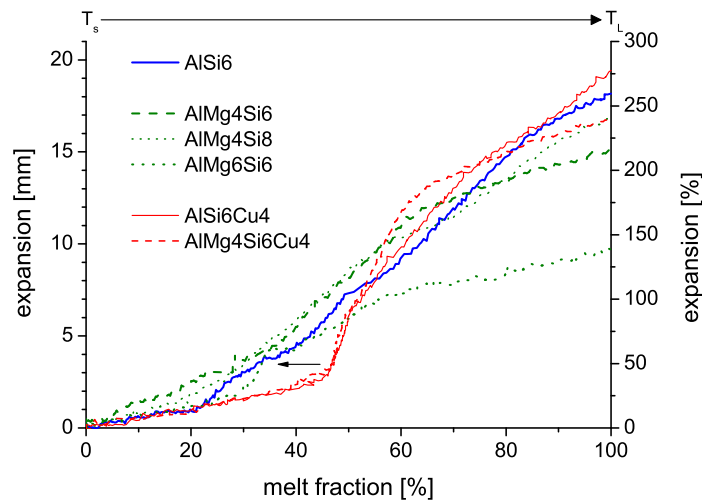


Figure 5: Expansion curves as a function of calculated melt fraction for 6 different alloys. The heating rate was  $1.2\text{ Ks}^{-1}$  in all cases.

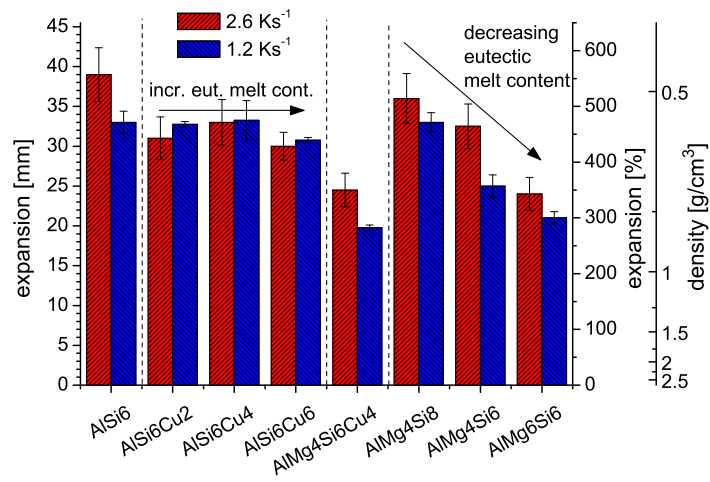
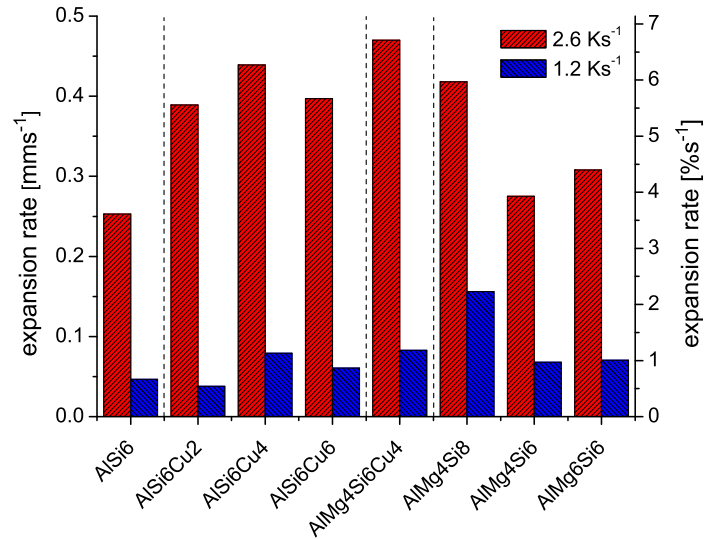
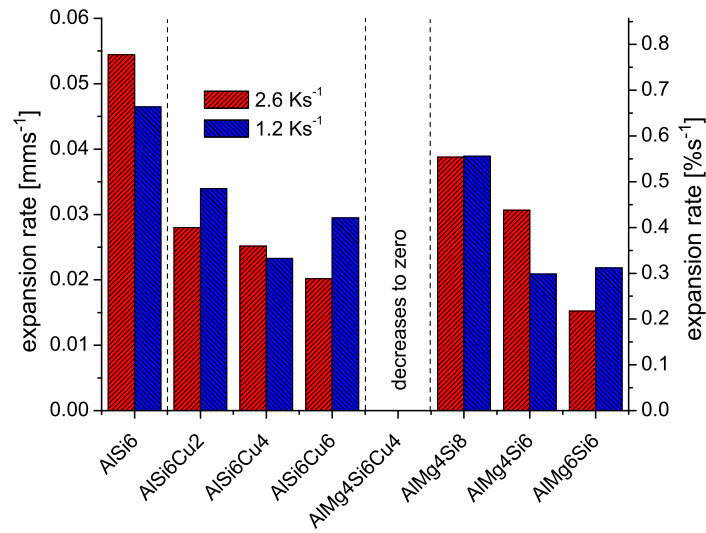


Figure 6: Maximum foam expansion values reached by the different alloys at both applied heating rates.



(a)



(b)

Figure 7: Expansion rates in the stage of constant expansion for different alloys and both heating rates, determined (a) shortly before reaching the final temperature of 630°C (corresponding to lines (1) and (3) in Fig. 3), (b) in the isothermal expansion stage (corresponding to lines (2) and (4) in Fig. 3).

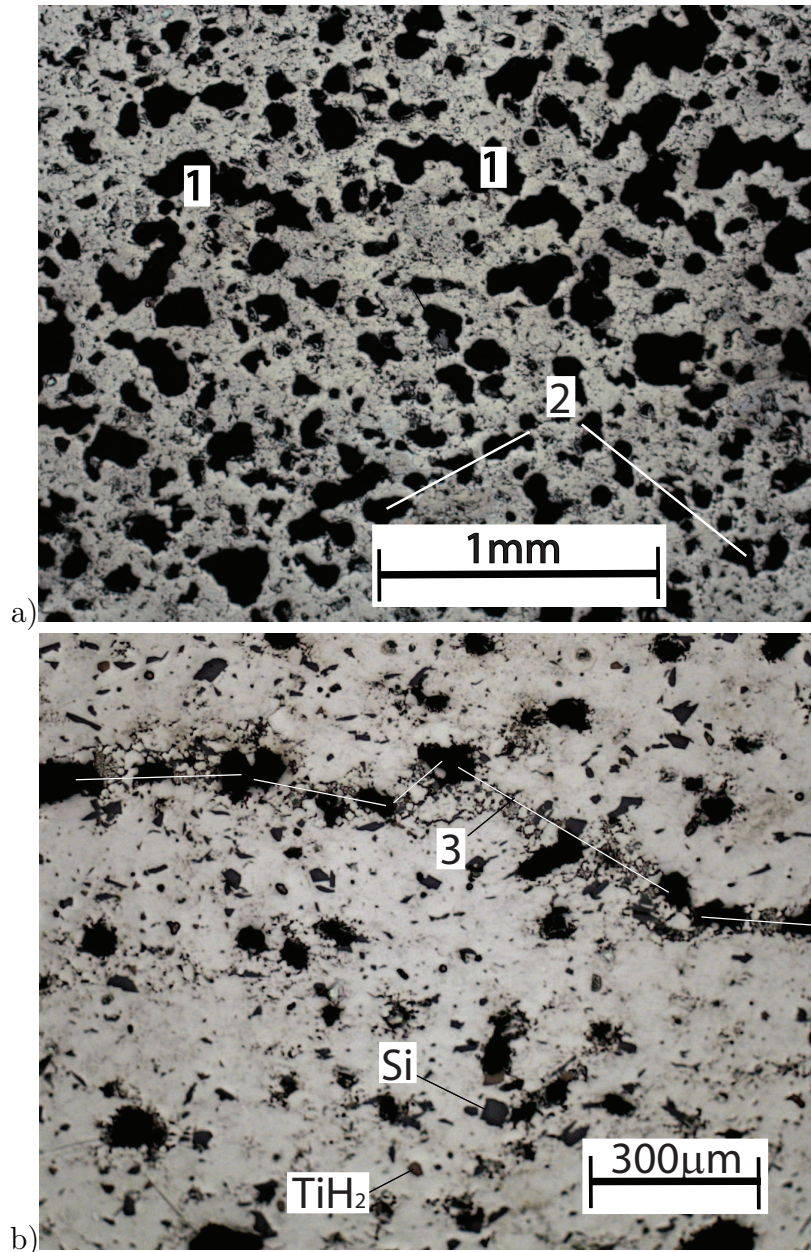


Figure 8: a) Typical early stage pore structure ( $P_{2D} = 31.7\%$ , alloy AlMg4Si6) showing the characteristic arrays of pores (2) and larger pores with irregular shape that emerged from those arrays (1). b) Close-up of transition regime between individual pore arrays (3) and larger pores surrounded by melt-rich zone in an earlier stage (3) ( $P_{2D} = 7.8\%$ , alloy AlSi6Cu4). Compaction direction is from top to bottom in both cases.

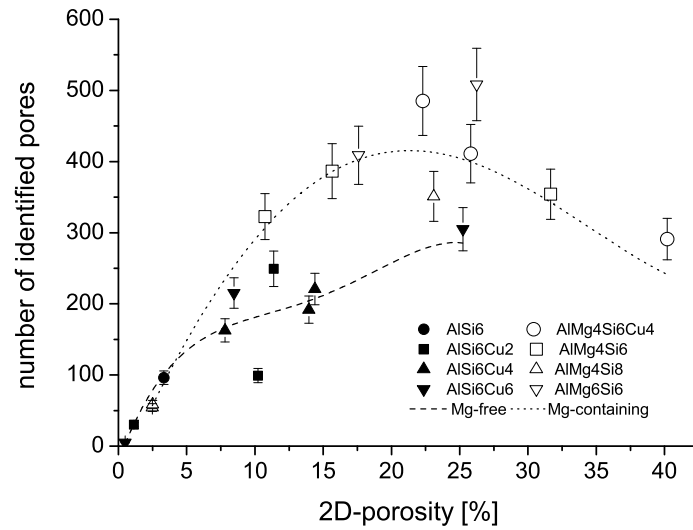


Figure 9: Number of pores (area  $> 450 \mu\text{m}^2$ ) per precursor volume as a function of porosity for different alloys. Trend lines for Mg-free and Mg-containing alloys are given.

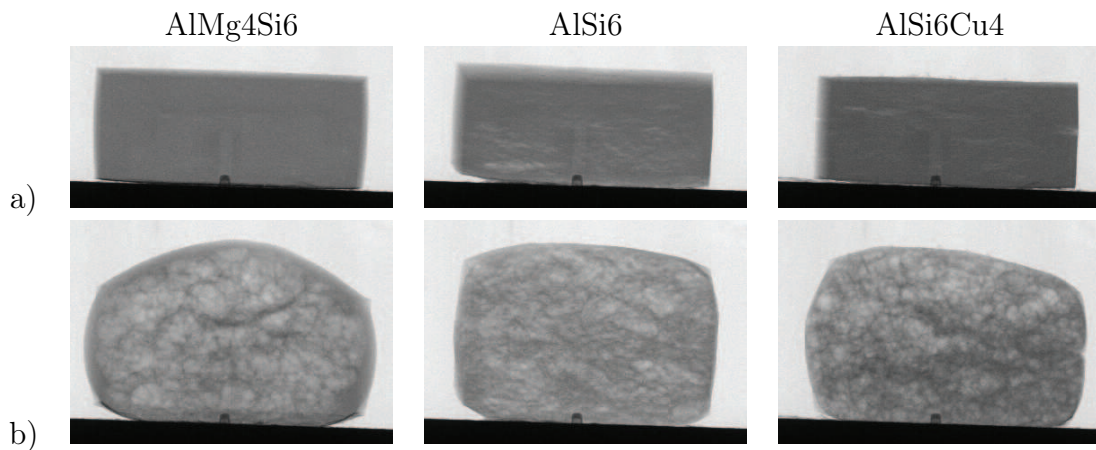


Figure 10: X-ray radiographs of two different foaming stages of the alloys AlSi6 (middle), AlMg4Si6 (left) and AlSi6Cu4 (right), a) area expansion  $\approx 30\%$ , b)  $\approx 100\%$ . The compaction direction is from top to bottom. Sample width is 20 mm.

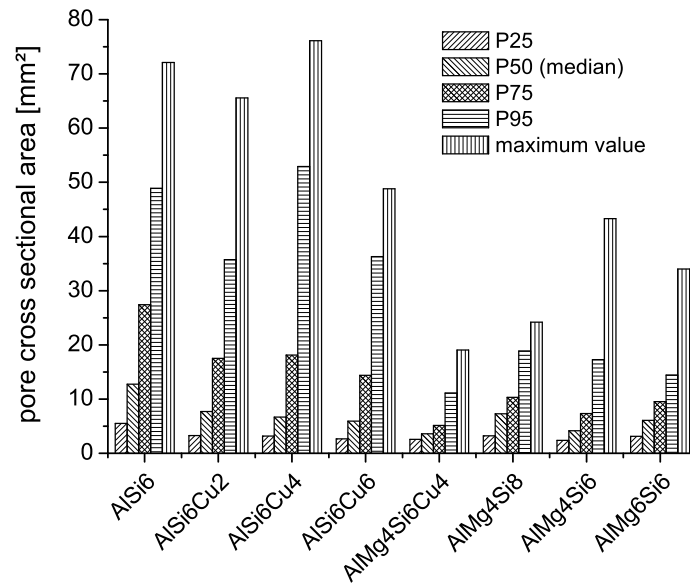


Figure 11: Pore area distributions of highly expanded foams made from the different alloys. Values  $P_n$  specify the cross section not exceeded by a given number fraction  $n\%$  of the pores. The smaller  $P_n$  are, the finer the foam. Heating rate was  $2.6 \text{ Ks}^{-1}$ .

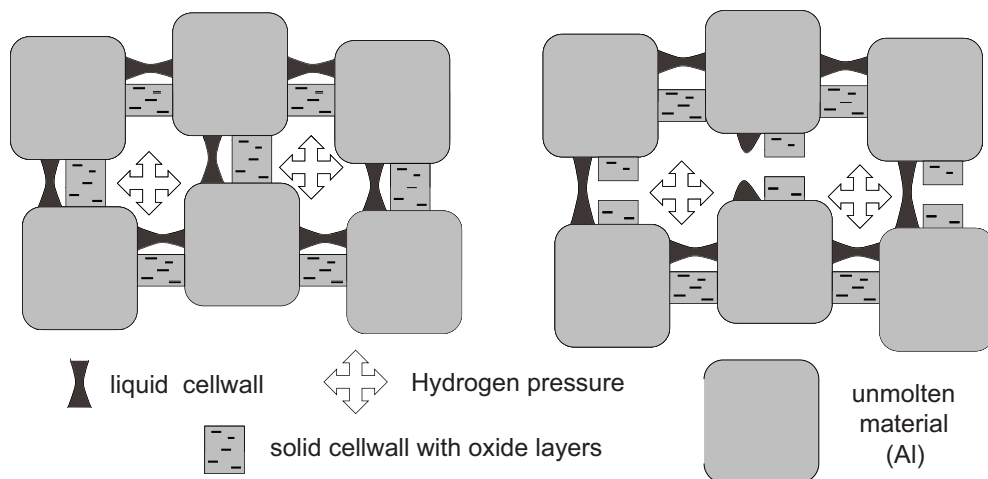


Figure 12: Sketch of pore coalescence in the semisolid state via rupture of either solid or liquid cell walls.



Figure 13: Photographic image of a foam made from AlMg<sub>4</sub>Si<sub>8</sub> alloy, showing a uniform pore structure.